Journal of Power Sources 195 (2010) 7974–7982

Contents lists available at ScienceDirect

Journal of Power Sources

journal homepage: www.elsevier.com/locate/jpowsour

Combustion synthesized $Nd_{2-x}Ce_xCuO_4$ (x = 0–0.25) cathode materials for intermediate temperature solid oxide fuel cell applications

A.P. Khandale, S.S. Bhoga*

Department of Physics, RTM Nagpur University, Nagpur 440033, Maharashtra, India

ARTICLE INFO

Article history:
Received 13 April 2010
Received in revised form 31 May 2010
Accepted 7 June 2010
Available online 23 June 2010

Keywords:
Cathode
Mixed ionic and electronic conductor
Combustion process
Area-specific resistance
Solid oxide fuel cell

ABSTRACT

It is found that the solid solubility of Ce in $Nd_{2-x}Ce_xCuO_{4\pm\delta}$ is limited up to x = 0.2. A semiconductor to metallic transition is observed at 600 °C in d.c. conductivity data, which coincides with a transition in temperature-dependent area-specific resistance (ASR). $Nd_{1.8}Ce_{0.2}CuO_{4\pm\delta}$ is thermodynamically and chemically stable against gadolinia-doped ceria (GDC) up to 1200 °C. On the other hand, it reacts with a yttria-stabilized zirconia electrolyte to form $Nd_2Zr_2O_7$. At 700 °C, the ASR of a $Nd_{1.8}Ce_{0.2}CuO_{4\pm\delta}$/GDC/$Nd_{1.8}Ce_{0.2}CuO_{4\pm\delta}$ cell sintered at 800 °C is 0.13 ohm cm^2, and the ASR proportionally improves with increase in the sintering temperature of the electrochemical cell. The improved ASR and electrochemical performance are attributed to the nanocrystalline nature of the cathode material.

© 2010 Elsevier B.V. All rights reserved.

1. Introduction

Solid oxide fuel cells (SOFCs), which convert chemical energy directly into electrical energy, have been viewed as promising new power-generating systems and true multi-fuel energy devices [1]. Conventional SOFCs, however, exhibit major disadvantages, such as cell-cracking, the formation of non-conducting compound(s) at electrode/electrolyte interfaces, and the need for expensive non-metallic interconnects. The drawbacks are mostly due to extremely high operating temperatures. Consequently, intermediate temperature solid oxide fuel cells (ITSOFCs) have gained increased importance. Nevertheless, achieving high cell performance at reduced temperatures has posed a great challenge for engineers and scientists engaged in SOFC development activities.

In the past, the utility of the cathode material, lanthanum strontium manganite (LSM), was limited due to its chemical reactivity with yttria-stabilized-zirconia (YSZ) [2]. Furthermore, it has been reported that the performance of LSM reduces rapidly on lowering of the operating temperature due to its poor ionic conductivity at such temperatures. Recently, $La_{1-x}Sr_xCo_{1-y}Fe_yO_{3-\delta}$ (LSCF) compounds have been proposed as alternative cathode materials for ITSOFCs [3,4]. The utility of LSCFs has, however, been limited due to the lack of chemical stability and a thermal expansion coefficient (TEC) that is incompatible with YSZ.

A potential cathode material must exhibit electronic as well as oxygen-ion conductivity to increase the triple-phase boundary (TPB) to enhance the efficiency of SOFCs. In addition, the material should exhibit good catalytic activity and compatible mechanical properties. Consequently, mixed ionic and electronic conductors (MIECs) have attracted a great deal of attention. Many mixed oxides of the form A_2BO_4 (A = rare earth, alkaline earth; B = transition metal) that crystallize with the tetragonal K_2NiF_4-type structure (space group *I4/mmm*) have received renewed interest. Such A_2BO_4 oxides have been of considerable interest due to adequate oxygen conduction, strong electrocatalytic activity towards the oxygen reduction and TECs comparable with those of conventional electrolytes [5,6]. The K_2NiF_4-type structure has an outer intergrowth of alternating perovskite (ABO_3) and rock-salt (AO) layers stacked along the tetragonal *c*-axis. Excess oxygen ions can be incorporated in the form of interstitial species into the rock-salt layer, without the compensation by cation vacancies observed in the ABO_3 type materials [7–10].

Significant mixed ionic and electronic conductivities with appreciable electrocatalytic activity have been found in Ln_2NiO_4 and Ln_2CuO_4 systems that have the K_2NiF_4-type structure [11–16]. In addition, the thermochemical stability of K_2NiF_4-type manganites, ferrites, cuperates and nickelates has been reported to be higher than those of the corresponding perovskite-type oxides [15]. The Co- and Fe-containing K_2NiF_4 compounds have recently been studied extensively [17,18]. Although the total conductivity and the TEC of $La_{2-x}Sr_xCuO_{4\pm\delta}$ materials are fairly satisfactory, the materials exhibit rather high area-specific resistances (ASRs) [16,19]. On the other hand, the ASR of a $Nd_{1.7}Sr_{0.3}CuO_4$ cathode on a samarium-

* Corresponding author. Tel.: +91 9822366066; fax: +91 7122500736.
E-mail address: msrl.physics1@gmail.com (S.S. Bhoga).

0378-7753/$ – see front matter © 2010 Elsevier B.V. All rights reserved.
doi:10.1016/j.jpowsour.2010.06.044

doped ceria (SDC) electrolyte has been found to be satisfactory [11]. Preliminary studies of $Nd_{2-x}Ce_xCuO_{4\pm\delta}$ ($0 \le x \le 0.2$) with both $Ce_{0.9}Gd_{0.1}O_{1.95}$ (GDC) and $La_{0.9}Sr_{0.1}Ga_{0.8}Mg_{0.2}O_{3\pm\delta}$ (LSGM) electrolytes have reported poor performances [10]. The authors have attributed the poor electrochemical performance to coarse and uneven particles.

In particular, the solid solutions $Nd_{2-x}Ce_xCuO_{4\pm\delta}$ ($0 \le x \le 0.2$) have been of special importance due to extrinsically created electron charge carriers, after doping with Ce. Their super-conducting transition in them has been found to be dependent on x. The crystal structure of $Nd_{2-x}Ce_xCuO_{4\pm\delta}$ is T′-type tetragonal and has copper–oxygen planes of CuO_2. In these planes, the copper ions have a square oxygen-ion neighbourhood (O1 site), and a sandwich is formed by the layers of oxygen ions (O_2 sites) interspersed with neodymium-cerium ions [20]. Accordingly, there are four possible modifications of tetragonal structures, T, T′, T* and O, for A_2BO_4 compounds [21,22]. The solid solutions of $Nd_{2-x}Ce_xCuO_{4\pm\delta}$ have invariably been prepared by solid-state reaction at very high temperatures (>1200 °C) for long periods of time (>40 h) [11,15]. A close scrutiny of the literature revealed that $Nd_{2-x}Ce_xCuO_{4\pm\delta}$ has received negligible attention for cathode applications in ITSOFCs.

There is sufficient scope for preparing $Nd_{2-x}Ce_xCuO_{4\pm\delta}$ ($0 \le x \le 0.2$) oxides through chemical routes to improve the electrochemical properties for ITSOFC cathode applications. In this work, various compositions of $Nd_{2-x}Ce_xCuO_{4\pm\delta}$ ($0 \le x \le 0.25$) are prepared by means of the acetate combustion technique. The prepared samples are characterized using X-ray powder diffraction, scanning electron microscopy and four-probe d.c. conductivity measurements. In addition, electrochemical impedance spectroscopy (EIS) studies are carried out on the symmetric cells $Nd_{1.8}Ce_{0.2}CuO_{4\pm\delta}$/GDC/$Nd_{1.8}Ce_{0.2}CuO_{4\pm\delta}$ sintered at 800 and 1200 °C.

2. Experimental

The initial reagents, namely cerium acetate, neodymium acetate and copper acetate, were procured from Aldrich Chemicals, USA and have a purity of >99.9%. All the reagents were dried at 120 °C for 6 h to remove any traces of moisture present. The reagents were dissolved in double-distilled deionised water separately in the required stoichiometric ratios. All the solutions were then mixed in a single corning flask. The homogeneous aqueous solution was then heated at 100 °C while subjecting it to a constant stirring using a rota-mantle to facilitate evaporation of the water. The resulting precipitate was then charred at about 250 °C by introducing it to an electric muffle furnace. It took >12 h to complete the entire procedure.

The residue obtained was then pulverized to form powders. Pellets of diameter and thickness 9 and 1–2 mm, respectively, were obtained by uniaxially compressing the ground powder at a pressure of 3 tons cm^{-2} with a Specac (UK) stainless-steel die-punch and hydraulic press. The resulting pellets were initially calcined at 800 °C for 4 h in an electric furnace. Subsequently, they were crushed, and pellets were made in a similar manner as described above before final sintering at 1000 °C for 4 h. The samples were allowed to cool to room temperature in the furnace.

All the prepared samples were subjected to structural characterization by X-ray powder diffraction (XRD) with a PANalytical X'pert PRO (Philips, the Netherlands) instrument that employed Cu Kα radiation. A curved graphite crystal was used as a monochromator. The X-ray diffraction measurements were carried out in a 2θ range from 10 to 80° with a step size and time per step of 0.020° and 5 s, respectively. The XRD data were refined with X'pert Highscore plus software. The sintered densities of all the samples were determined using Archimedes' principle. The microstructures of the sintered samples were examined with a JEOL JSM-6380A scanning electron microscope. Microhardness was measured by the Vickers indentation technique (HMV-2 microhardness tester, Shimadzu, Japan).

A thin platinum film on both flat surfaces of the sintered pellet was obtained by d.c. sputtering and resulted in good ohmic contacts for d.c. electrical conductivity measurements. Prior to the conductivity measurements, the sample was spring-loaded in a ceramic cell holder (Amel, Italy) and heated to 700 °C for 1 h to homogenize the charge carriers. The resistance during the cooling cycle was measured as a function of temperature using the four-probe method with a computer-controlled Keithley 6221 current source and a 2182A nanovoltmeter in delta mode. The temperature of the sample during the measurement was controlled with an accuracy of ±1 °C with a Eurotherm 2216e temperature controller. The tip of a calibrated thermocouple was kept in the vicinity of the sample to measure its actual temperature. The oxygen partial pressure around the cell during the conductivity measurements was maintained using electronic mass flow meters and controllers (Teledyne-Hastings, USA). Nitrogen was used as the carrier gas.

For electrochemical investigations, the initial slurry/ink of the $Nd_{1.8}Ce_{0.2}CuO_{4\pm\delta}$ cathode was obtained as follows. A gram of $Nd_{1.8}Ce_{0.2}CuO_{4\pm\delta}$ powder was mixed with 3 wt.% polyvinyl buteral binder, sodium free corn oil, and ethyl methyl ketone. The mixture was then ball-milled using a Pulverisette-6 (Fritsch Germany) for 1 h with 300 revolutions per minute. Thirty-five tungsten carbide balls of diameter 10 mm and 80-ml bowl of the same material were used. The GDC (10 mol. % gadolinium-doped ceria) nano-powder (Aldrich, USA) was pressed in a similar manner to obtain pellets of diameter 9 mm and thickness 1–2 mm. They were then sintered at 1400 °C for 6 h. A sintered density of about 96% was achieved. Both flat surfaces of the GDC pellet were then roughened with # 60 grid paper and cleaned with acetone. The slurry/ink of each cathode material was then spin-coated at 3000 rpm for 60 s on both flat surfaces of the sintered GDC electrolyte to obtain the following symmetric cell configurations.

$Nd_{1.8}Ce_{0.2}CuO_{4\pm\delta}$/GDC/$Nd_{1.8}Ce_{0.2}CuO_{4\pm\delta}$

The symmetric cells were initially baked at 600 °C for 2 h to burn out the organic binders, and finally sintered at 800 and 1200 °C for 2 h. The cells sintered at 800 and 1200 °C are abbreviated as cell-800 and cell-1200, respectively.

Electrochemical impedance measurements on the sintered symmetric cells were carried out using a computer-controlled Solartron 1255B FRA in combination with a Solartron SI 1287 electrochemical interface. Prior to the impedance measurement, the spring-loaded samples were heated to 700 °C (T_1) for 1 h as shown in Fig. 1. During the cooling cycle, a dwell time of 30 min was allowed at each set temperature (T_2, T_3, T_4, ...) to ensure that thermal equilibrium was achieved in the cells. Ten minutes prior to the end of the dwell time (t_{s1} in Fig. 1), the real and the imaginary parts of the impedance were measured as a parametric function of frequency and temperature in the range of 0.01–1 × 10^6 Hz and 480–700 °C, respectively, with a signal amplitude of 50 mV. The concentration of O_2 gas (P_{O_2}) was monitored as discussed previously. The EIS data obtained were analyzed using software developed by Scribner advanced software for electrochemical research and development.

To evaluate the chemical compatibility of the $Nd_{1.8}Ce_{0.2}CuO_{4\pm\delta}$ cathode with the GDC and YSZ electrolytes, the symmetric cells were sintered at 1200 °C for 48 h. The interface powder was then subjected to XRD to identify the phases present.

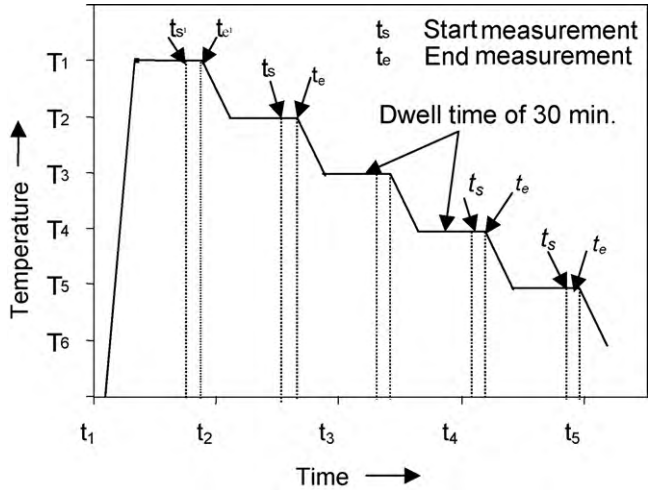

Fig. 1. Temperature profile during EIS measurements.

3. Results and discussion

3.1. X-ray powder diffraction

Typical X-ray powder diffraction (XRD) patterns of $Nd_{2-x}Ce_xCuO_{4\pm\delta}$ with $x = 0$, 0.20 and 0.25 are shown in Fig. 2(a)–(c), respectively. In general, all the diffracted lines were broader than the usual ones. This broadening is attributed to the nanocrystalline nature of the materials. The obtained XRD data were profile-fitted with X'pert Highscore plus software before indexing. A close look at Fig. 2(a) reveals that all the characteristic diffracted lines match closely with the Joint Committee on Powder Diffraction Standard (JCPDS) data (File No. 01-084-2177) that correspond to pure Nd_2CuO_4. Lines corresponding to either the initial reagents or any intermediate compound(s) are not present. Similarly, all diffracted lines appeared appear in Fig. 2(b) match closely the JCPDS data for tetragonal Nd_2CuO_4, with only small deviations. No lines due to initial reagents are seen. On the other hand, in addition to the lines associated with Nd_2CuO_4 (Fig. 2(c)), a few weak characteristic diffracted lines due to CeO_2 are present in the case of $x = 0.25$. Nevertheless, the absence of lines corresponding to either pure reagents or intermediate phases confirms the formation of single-phase tetragonal $Nd_{2-x}Ce_xCuO_{4\pm\delta}$ solid solutions up to $x \leq 0.2$. Furthermore, the cerium precipitated out of the $Nd_{1.8}Ce_{0.2}CuO_{4\pm\delta}$ matrix for $x = 0.25$. These results are in good agreement with the results of Spinolo et al. [23]. To ascertain the formation of a solid solution and its consequence on the host lattice structure, the lattice cell constants for all samples under study were determined using Unitcell computer software [24]. The obtained lattice cell constants, $a = 3.956$ and $c = 12.208$ Å, for pure Nd_2CuO_4 are in good agreement with the reported values of $a = 3.944$ Å and $c = 12.169$ Å [25]. The variation of lattice cell constants a and c of $Nd_{2-x}Ce_xCuO_{4\pm\delta}$ with x is depicted in Fig. 3. It can be seen that the lattice cell constant c decreases linearly up to $x = 0.2$, and remains unchanged for $x > 0.2$. These results substantiate the solid solubility limit up to $x = 0.2$ discussed above. On the other hand, there is a negligible change in the lattice constant a with increase in x. The Nd_2CuO_4 lattice contraction along the c-axis due to Ce doping has been observed earlier [20]. According to the literature, Ce remains tetravalent and occupies the 8-coordinated Nd^{3+} site in a T′ type Nd_2CuO_4 structure. The ionic radius ($r_g = 0.97$ Å) of 8-coordinated Ce^{4+} [25] is smaller than that of the 8-coordinated host Nd^{+3} ($r_h = 1.01$ Å) [20]. Thus, the partial substitution of the latter for the former leads to Nd_2CuO_4 lattice contraction. Because of the absence of apical oxygen and the existence of a single CuO_2 plane in the unit cell of the T′ type Nd_2CuO_4 crystal structure, the Cu ions are 4-coordinated. Consequently, the coupling between the CuO_2 layers along the c-axis is expected to be weaker than along the a-axis and thereby leads to an anisotropic lattice contraction. Voronin et al. [20] have given a detailed justification for the lattice contraction along the c-axis due to partial replacement of Nd^{3+} for Ce^{4+} in Nd_2CuO_4.

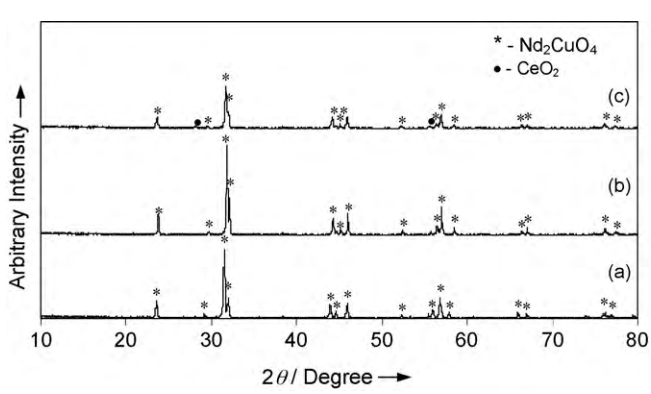

Fig. 2. X-ray powder diffraction patterns of $Nd_{2-x}Ce_xCuO_{4\pm\delta}$ with (a) $x = 0$, (b) $x = 0.2$ and (c) $x = 0.25$.

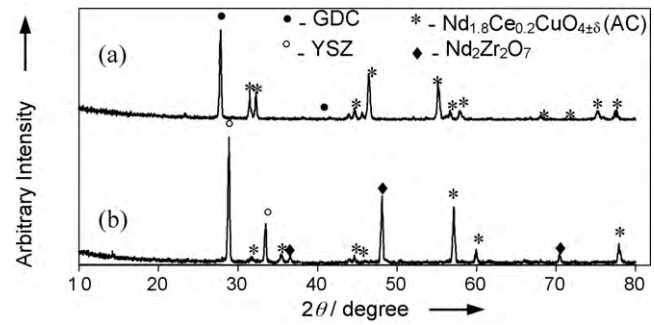

Fig. 3. X-ray powder diffraction patterns of $Nd_{1.8}Ce_{0.2}CuO_{4\pm\delta}$ with (a) GDC and (b) YSZ sintered at 1000 °C for 45 h.

Table 1 compares the crystallite size of all compositions under study, determined using the X'pert Highscore plus software based on the following expression:

$$t = \frac{0.9\lambda}{\beta \cos\theta_B} \quad (1)$$

where t, λ, and θ_B are the thickness of the crystallite, X-ray wavelength and Bragg's angle, respectively. Here, β is obtained by:

$$\beta^2 = {\beta_m}^2 - {\beta_s}^2 \quad (2)$$

where β_m and β_s are the measured and standard full width at half maxima (FWHM), respectively, of the diffracted line. The XRD pattern, obtained by running the experiment on a standard silicon sample provided by PANalytical (Netherlands), is used to estimate

Table 1
Comparison of crystallite size, lattice strain, sinter density and microhardness number of $Nd_{2-x}Ce_xCuO_{4\pm\delta}$ with $x = 0$–0.25.

Composition	C_s (Å)	Density (%)	*HV*
Nd_2CuO_4	770	88.56	635
$Nd_{1.95}Ce_{0.05}CuO_4$	772	84.00	627
$Nd_{1.9}Ce_{0.1}CuO_4$	1056	80.57	619
$Nd_{1.85}Ce_{0.15}CuO_4$	1842	81.12	622
$Nd_{1.8}Ce_{0.2}CuO_4$	1964	80.92	614
$Nd_{1.75}Ce_{0.25}CuO_4$	1620	89.33	532

C_s – crystallite size; HV – microhardness number.

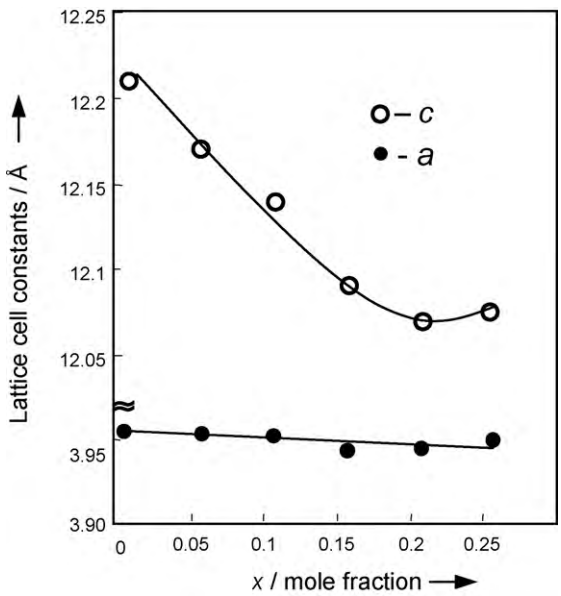

Fig. 4. Variation of lattice cell constants, *a* and *c*, with *x* in $Nd_{2-x}Ce_xCuO_{4\pm\delta}$.

the value of β_s. A close scrutiny of the data in Table 1 suggests that all the compositions under study are nanocrystalline materials. Furthermore, the crystallite size increases with an increase in *x* within the solid solubility limit. By contrast, the grain size of samples with $x = 0.25$ is smaller than that of $x = 0.20$. The precipitation of CeO_2 in the $Nd_{1.8}Ce_{0.2}CuO_{4\pm\delta}$ matrix hinders the grain growth, thereby resulting in relatively smaller grains. This result also supports the observed solid solubility limit up to $x = 0.2$. From Table 1, it can be seen that the sintered density of $Nd_{2-x}Ce_xCuO_{4\pm\delta}$ decreases with *x*. The reduction in sinter density is attributed to the increased crystallite size (Table 1). A close inspection of Table 1 reveals that the microhardness number increases commensurately with sintered density of $Nd_{2-x}Ce_xCuO_{4\pm\delta}$. By contrast, the low microhardness number of $Nd_{1.75}Ce_{0.25}CuO_{4\pm\delta}$, in spite of the high sinter density, is attributed to inferior grain glue/adhesion resulting from the bi-phase mixture. The homo-junctions, i.e., the interfaces between same grains (grain boundary), are chemically strong and thereby exhibit better adhesion (glue) between the grains. On the other hand, hetero-junctions are chemically weakly bound. These factors are responsible for low microhardness of the bi-phase composition, i.e., $x = 0.25$.

The XRD patterns of $Nd_{1.8}Ce_{0.20}CuO_{4\pm\delta}$ + GDC and $Nd_{1.8}Ce_{0.20}CuO_{4\pm\delta}$ + YSZ sintered at 1200 °C for 48 h are shown in Fig. 4(a) and (b). All the diffraction lines in Fig. 4(a) closely match with those of either $Nd_{1.8}Ce_{0.2}CuO_{4\pm\delta}$ or GDC. On the other hand, in addition to the diffracted lines due to $Nd_{1.8}Ce_{0.2}CuO_{4\pm\delta}$ and YSZ, a few lines corresponding to the intermediate compound $Nd_2Zr_2O_7$ are clearly seen in Fig. 4(b). These results suggest that $Nd_{1.8}Ce_{0.20}CuO_{4\pm\delta}$ exhibits excellent chemical stability with GDC as compared with YSZ. Thus, GDC is selected for further electrochemical studies of the $Nd_{1.8}Ce_{0.2}CuO_{4\pm\delta}$ cathode.

3.2. Scanning electron microscopy

Scanning electron microphotographs (SEM) of $Nd_{2-x}Ce_xCuO_{4\pm\delta}$ with $x = 0.05$–0.2 and 0.25 are displayed in Fig. 5(a)–(e), respectively. For all compositions in general, 90% of the cleaved surface consists of trans-granular cleavages, and the other 10% consists of voids and grain-boundaries. A close look at the figures also reveals that the grain size increases with increase in *x* of $Nd_{2-x}Ce_xCuO_{4\pm\delta}$. Furthermore, the grains are elongated with increased cerium content.

The SEM photograph of a fractured surface across the electrode/electrolyte interface of the symmetric cell-800 after four thermal cycles is depicted in Fig. 6. As seen from the figure, the electrode and electrolyte form intimate contact across the interface. Moreover, electrode/electrolyte interface is homogeneous. Despite four thermal cycles at 800–20 °C, no cracks or separations between the electrode and electrolyte is found at the interface. The electrode layer thickness is approximately 62.7 μm. A close look at Fig. 6(b) reveals that the nano-crystallites of $Nd_{1.8}Ce_{0.2}CuO_{4\pm\delta}$ have agglomerated to form a porous electrode. Furthermore, such agglomerates are uniformly distributed in such a way that the electrode structure becomes highly porous. Sintering of a symmetric cell at 1200 °C facilitates the fusion of nanocrystalline grains of $Nd_{1.8}Ce_{0.2}CuO_{4\pm\delta}$, leading to grain growth (Fig. 6(c)). By contrast, the electrolyte is nonporous, i.e., highly dense (Fig. 6(a)).

3.3. d.c. conductivity

The variation of d.c. conductivity with temperature for all the samples under study is shown in Fig. 7. $Nd_{2-x}Ce_xCuO_{4\pm\delta}$ with $x = 0.1$, 0.15 and 0.2 exhibits a positive temperature coefficient (PTC) to negative temperature coefficient (NTC) transition at about 625 °C. The absence of the transition for pure Nd_2CuO_4 and $x = 0.05$ is in line with other reported results [21]. Below this transition temperature, all the samples obey the Arrhenius law, i.e.,

$$\sigma = \sigma_0 \exp\left(\frac{-E_a}{kT}\right), \tag{3}$$

where σ_0, *k*, *T* and E_a are the pre-exponential factor, Boltzmann constant, absolute temperature and activation energy, respectively. The variation of d.c. conductivity at 600 °C and activation enthalpy as a parametric function of *x* in $Nd_{2-x}Ce_xCuO_{4\pm\delta}$ is shown in Fig. 8 . The d.c. conductivity initially increases with an increase in Ce content, and attains a maximum for $x = 0.15$ and decreases thereafter. The activation energy follows an opposite behavior to that of the conductivity with *x*. The minimum activation energy composition coincides with the composition that has the maximum conductivity.

Intrinsically, electrons and holes can be produced in $Nd_2CuO_{4\pm\delta}$ lattice by the following two point defect equilibria [21]:

$$O_O \Leftrightarrow V_O^{\bullet\bullet} + 2e' + \frac{1}{2}O_2, \tag{4}$$

$$\frac{1}{2}O_2 \Leftrightarrow O_i'' + 2h^{\bullet}, \tag{5}$$

coupled with intrinsic ionization:

$$\text{nil} \Leftrightarrow e' + h \tag{6}$$

At intermediate P_{O_2} and temperature, $Nd_2CuO_{4\pm\delta}$ is almost stoichiometric in oxygen, and shows semiconducting behavior where the carriers are electrons and holes created by thermal promotion of electrons from the valence band to the conduction band according to Eqs. (5) and (6). At higher temperatures, however, the majority charge carriers are electrons created by the equilibrium Eq. (4) in the whole range of P_{O_2}. At the same time, there may be an overlapping of valence and conduction bands leading to a metallic behavior, i.e., the conductivity decreases with an increase in temperature (Fig. 7).

The partial substitution of Ce^{4+} for Nd^{3+} introduces extrinsic defects according to the following quasichemical reaction:

$$CuO + 2CeO_2 \rightarrow Cu_{Cu}{}^{x} + 2Ce_{Nd}{}^{\bullet} + 4O_o{}^{x} + 2e' + \frac{1}{2}O_2 \tag{7}$$

The electrons thus created are associated with the CuO_2 planes. The concentration of such extrinsically created electrons in CuO_2 planes increases with an increase in Ce concentration. The increase

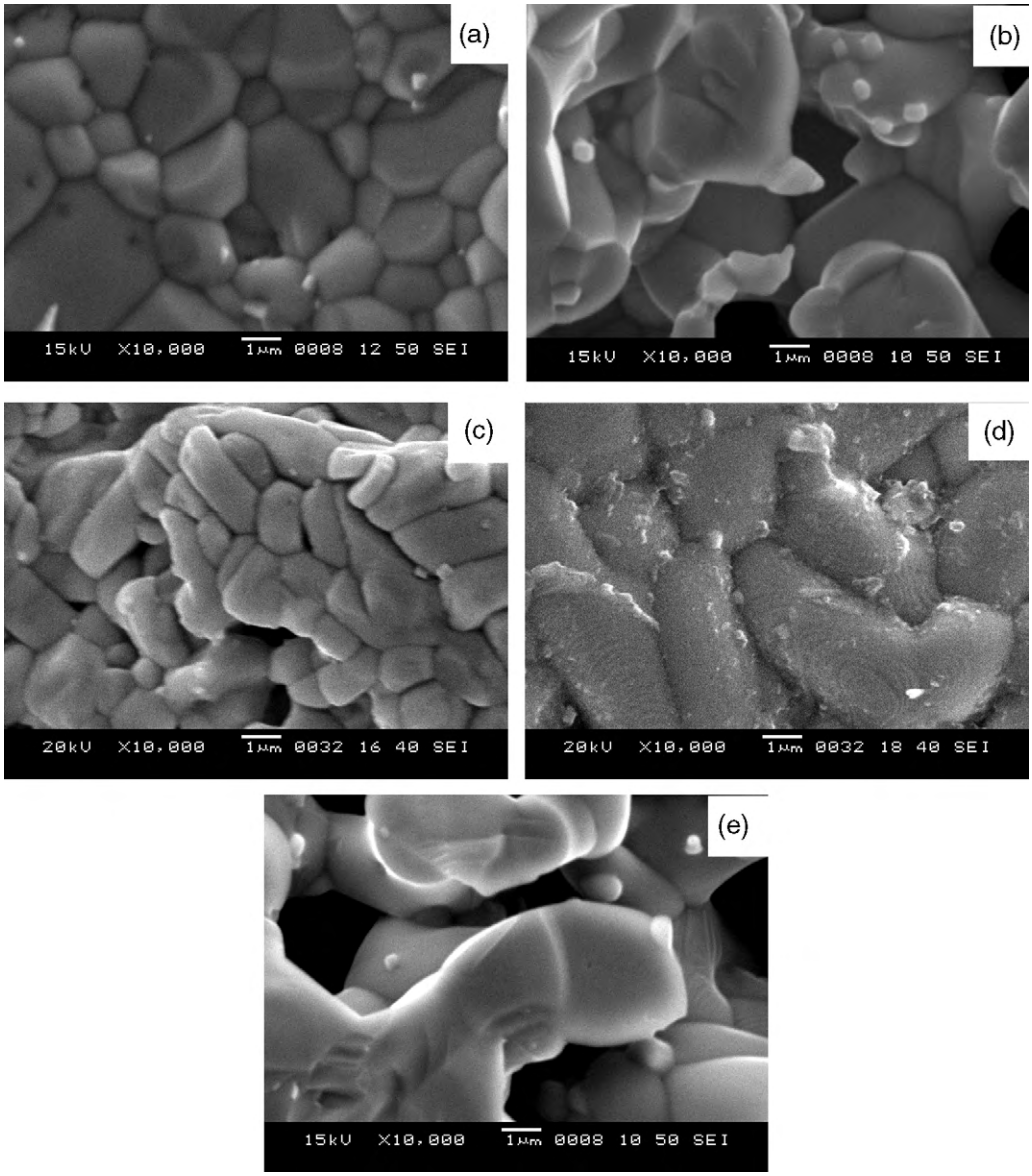

Fig. 5. Scanning electron microphotographs of $Nd_{2-x}Ce_xCuO_{4\pm\delta}$ with (a) $x = 0.05$, (b) $x = 0.1$, (c) $x = 0.15$, (d) $x = 0.20$, and (e) $x = 0.25$.

in electron concentration has been supported by Hall coefficient measurements by Takagi et al. [26]. Thus, the d.c. conductivity of $Nd_2CuO_{4\pm\delta}$ in the present study increases with Ce content. Singh et al. [27] have observed a relatively rapid increase in the content of the lattice oxygen of $Nd_{2-x}Ce_xCuO_{4\pm\delta}$ for $0.155 \leq x \leq 0.175$. According to their research, there exists a critical range of unit cell volume and oxygen content for a smooth super-conducting transition. Furthermore, there is a critical unit cell volume corresponding to $x = 0.15$. Below this concentration ($x \leq 0.15$), the electrostatic attraction amongst the lattice is strong enough to limit the removal of oxygen. These factors may be responsible for the maximum conductivity for $x = 0.15$ (Fig. 8). The variation of d.c. conductivity (at 650 °C) with log P_{O_2} depicted in Fig. 9 suggests that the electronic conductivity decreases with an increase in oxygen partial pressure. The very small d.c. conductivity that is dependent on oxygen partial pressure is in good agreement with previous works [20]. Although the d.c. conductivity is highest for $Nd_{2-x}Ce_xCuO_{4\pm\delta}$ with $x = 0.15$, the cathode composition with $x = 0.20$ is selected for electrochemical studies with GDC as the electrolyte because the solid solubility of the GDC electrolyte is up to $x = 0.2$. The solid solubility of the electrolyte in the cathode may affect the electrochemical performance.

3.4. Electrochemical impedance spectroscopy

Typical complex impedance spectra of cell-800 at 660 and 480 °C are depicted in Fig. 10(a) and (b), respectively. In general, convoluted impedance spectra are observed. The impedance spectra shown in Fig. 10(a), analyzed using a computer program, show a clear semicircular arc in the low-frequency region. The incomplete semicircular arc in the high-frequency region is attributed to the limitation of the Solartron 1255B FRA for high frequencies (≤1 MHz). A close inspection of Fig. 10(b) reveals the presence of three semicircular arcs. The first low-frequency semicircular arc is due to the passage of current through the electrode and across the electrode/electrolyte interface and also complex electrode processes. The second semicircular arc in the mid-frequency domain is attributed to the grain-boundary contribution of the GDC electrolyte. The incomplete high-frequency semicircular arc is due to the bulk grain of GDC. The semicircular arc representing elec-

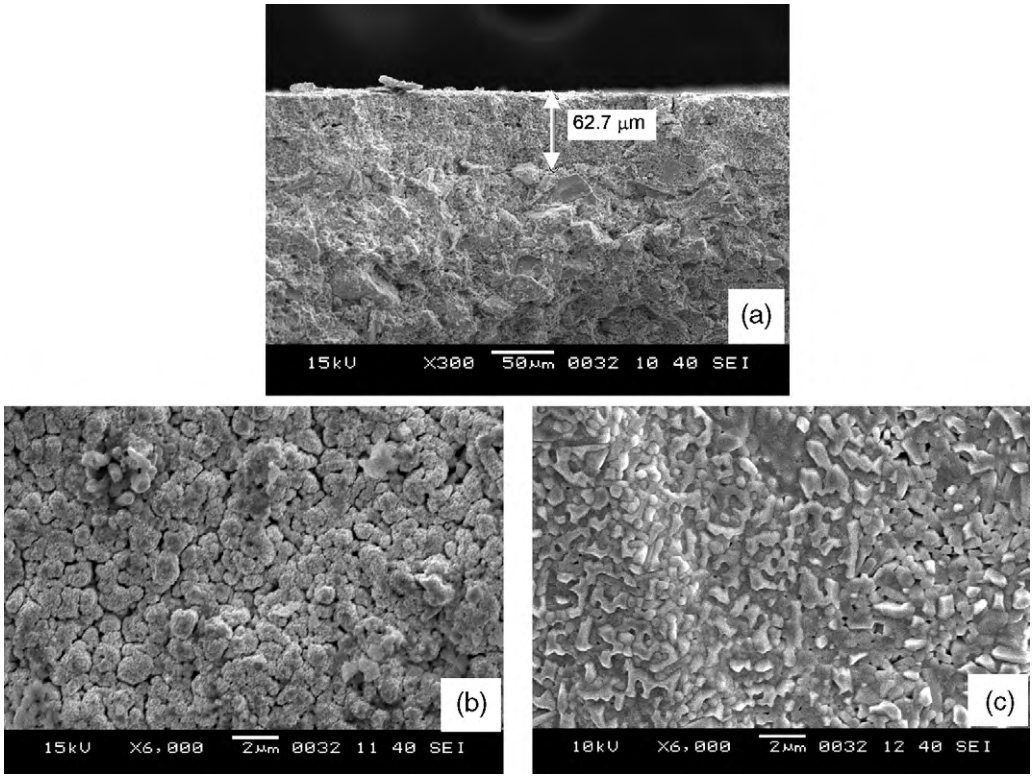

Fig. 6. Scanning electron microphotographs of (a) electrode/electrolyte interface of cell-800 and cathode surface of (b) cell-800 and (c) cell-1200.

trode polarization is characteristic of the reversible reduction of O_2 gas at the cathode, and subsequent migration of O^{2-} across the interface.

Complex impedance spectra of cell-1200 at 660, 680 and 700 °C are given in Fig. 11. In this case, two discernible semicircular arcs are present. In general, the real axis intercepts of all semicircular arcs increase with a decrease in temperature as expected, and indicate increased ASR as well as bulk resistance. The electrical equivalent circuit shown in Fig. 12, represents the impedance data for all symmetric cells under study. The constant phase element (CPE) in each circuit accommodates the depression in the semicircular arc due to the distributed relaxation time. R_{lead}, R_{elect} and R_{cath} represent the lead resistance, the resistance of the grain and grain boundary of electrolyte and the resistance of the cathode, respectively. $C_{elect.}$, and C_{dl} are the capacitances due to the grain, grain boundary and double-layer interface capacitor, respectively. The W in the parallel circuit representing the low-frequency arc is due to the Warburg impedance.

The electrolytic bulk conductivity, σ_{GDC}, at atmospheric pressure is obtained using Eq. (8),

$$\sigma_{GDC} = \frac{1}{R}\frac{t}{S}, \tag{8}$$

where t and S are the thickness and the surface area of the electrolyte respectively. The values of R were estimated from the complex impedance plots of the symmetric cell-800. The Arrhenius plot for GDC is shown in Fig. 13. The activation energy E_a = 0.88 eV

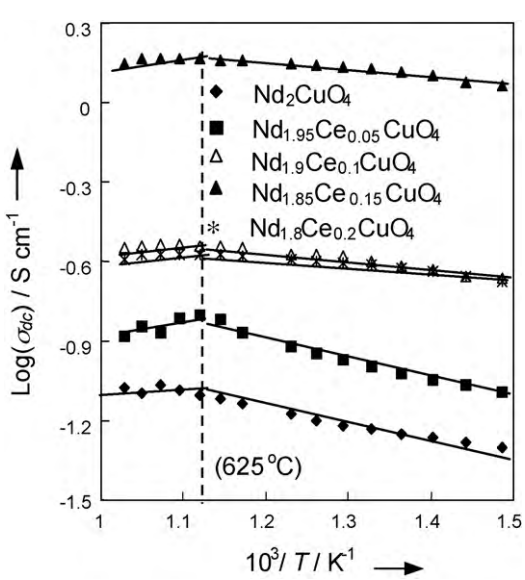

Fig. 7. Arrhenius plots for $Nd_{2-x}Ce_xCuO_{4\pm\delta}$ with x = 0–0.2.

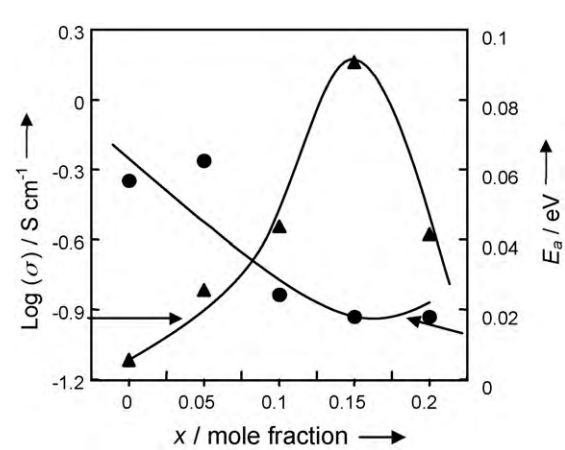

Fig. 8. Variation of log σ at 600 °C and activation enthalpy (E_a) with x for $Nd_{2-x}Ce_xCuO_{4\pm\delta}$.

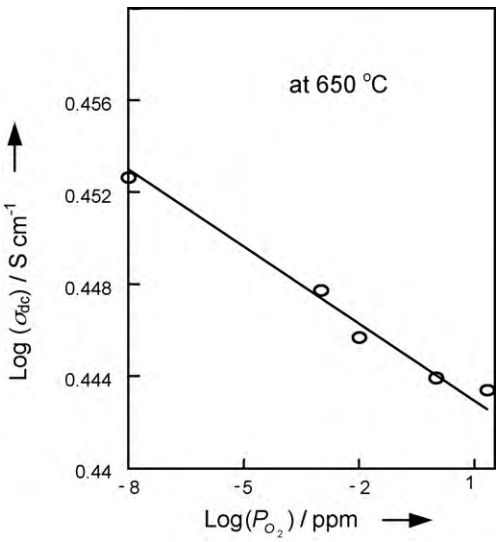

Fig. 9. Variation of d.c. conductivity at 650 °C for $Nd_{1.8}Ce_{0.2}CuO_{4\pm\delta}$ with P_{O_2}.

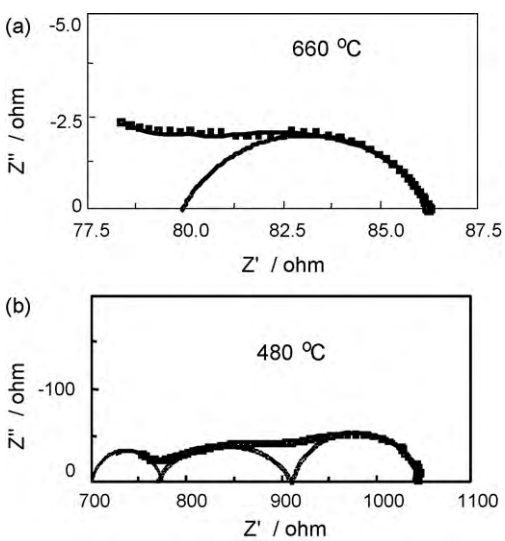

Fig. 10. Complex impedance plots for cell-800 at (a) 660 and (b) 480 °C.

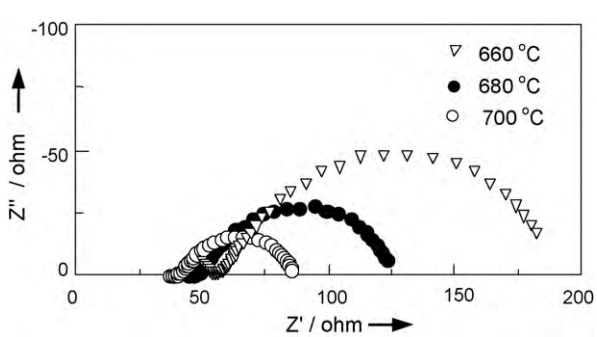

Fig. 11. Complex impedance plots at various temperatures for cell-1200.

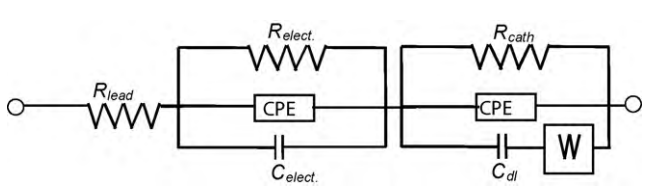

Fig. 12. Electrical equivalent circuit for symmetric cells.

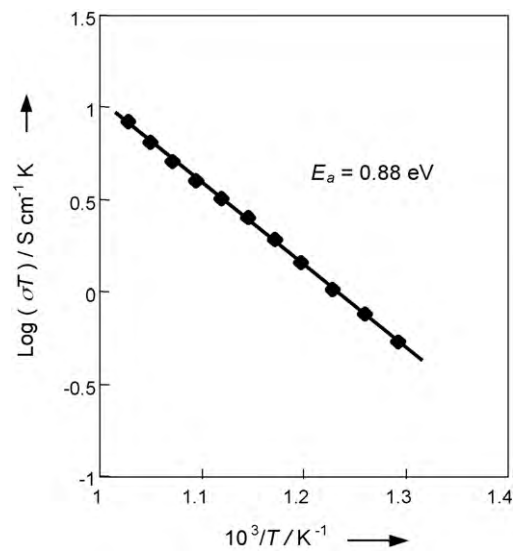

Fig. 13. Arrhenius plots for bulk conductivity of GDC electrolyte obtained from EIS on cell-800.

determined in the present work is in good agreement with the earlier reported value of E_a = 0.9 eV [28].

A comparison of the temperature-dependent ASR of cell-800 and cell-1200 is given in Fig. 14. A transition at approximately 620 °C is clearly seen in both cells. The observed transition temperature (T_c) matches closely with the $T_c \approx 625$ °C, corresponding to NTC to PTC transition (Fig. 7). The ASR below and above T_c obeys the Arrhenius law. Furthermore, the ASR and activation energy in the entire temperature range of the measurement are higher for cell-1200 than for cell-800. The sintering of the cell at a higher temperature (1200 °C) gives rise to grain growth, thereby reducing the number of pores in the cathode (Fig. 4). Both these factors reduce the catalytic activity and result in the high ASR and activation energy for cell-1200. The activation energies in the low-and high-temperature regions are compared in Table 2. The transition in the temperature-dependent ASR at 550 °C has been observed

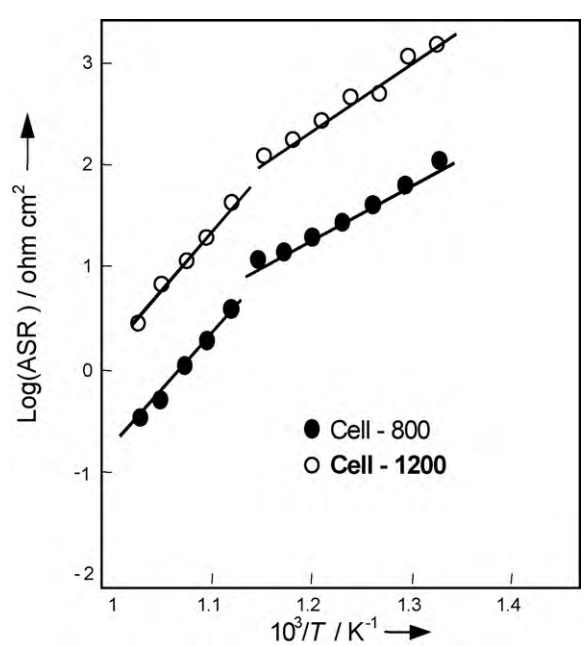

Fig. 14. Arrhenius plots of ASR of cell-800 and cell-1200.

Table 2
Comparison of ASR values determined in this study with values reported in the literature.

Sr #	Cathode	ASR (ohm cm^2)	T (°C)	E_a (eV)	Reference
1	$Nd_{1.7}Sr_{0.3}CuO_4$	0.24	700		[11]
2	$La_2Ni_{0.6}Cu_{0.4}O_{4+\delta}$	1.0	850		[19]
3	$Nd_{1.8}Ce_{0.2}CuO_4$	–	–	1.06 (LT) 1.44 (HT)	[10]
4	$Nd_{1.8}Ce_{0.2}CuO_4$	0.13	700	0.95 (LT) 1.73 (HT)	[a]

LT – low temperature region; HT – high-temperature region.
[a] Present study

by Soorie and Skinner [10]. The disparity between the values of T_c and E_a of the present study and reported values [10] (Table 2) is attributed to the variation in grain size and grain morphology that result from differences in the preparative methods.

The variation of the peak frequency (f_p) corresponding to the low-frequency semicircle in the complex impedance plane with temperature is depicted in Fig. 15 and suggests Arrhenius-like behavior. The change in slope at 620 °C coincides with the transition observed in the temperature-dependent ASR. The activation energy (E_a) is determined using the following relationship:

$$f_p = f_o \exp\left(\frac{E_a}{kT}\right), \quad (9)$$

where f_p, and f_o are the jump frequency and attempt frequency respectively. The E_a = 0.95 and 1.73 eV which correspond to the low- and high-temperature regions, respectively, and obtained from the relaxation frequency plot are in good agreement with those determined from the ASR plot (Table 2). These results indicate that the charge transfer within the electrode as well as across the electrode/electrolyte interface took place via the hopping mechanism.

The complex impedance plots at 650 °C for cell-800 under different d.c. biasing potentials are depicted in Fig. 16(a). In general, the ASR is reduce with an increased biasing potential (Fig. 16(a) and (b)). On the other hand, there is a negligible change in the electrolytic bulk resistance with the variation in d.c. biasing potential, as expected. The decrease in the ASR with increased d.c. potential is in agreement with previous studies [29].

The complex impedance plots for different values of P_{O_2} for cell-800 are shown in Fig. 17(a). The x-axis intercept corresponding to the low-frequency semicircular arc changes with P_{O_2}. On the other hand, the electrolytic bulk resistance/conductivity is least affected by changes in P_{O_2}. The linear dependence of log(ASR) on log(P_{O_2})

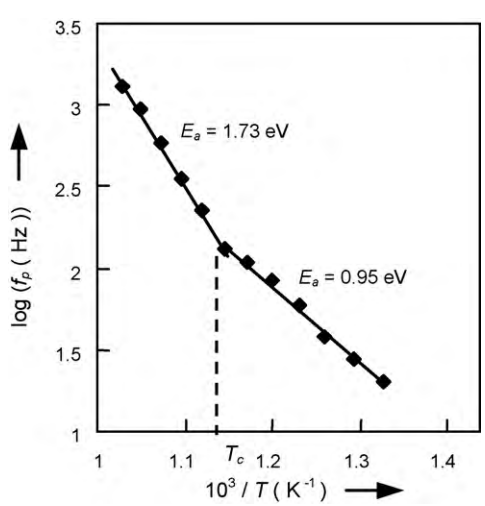

Fig. 15. Arrhenius plots of electrode relaxation frequency, f_p, obtained from cell-800.

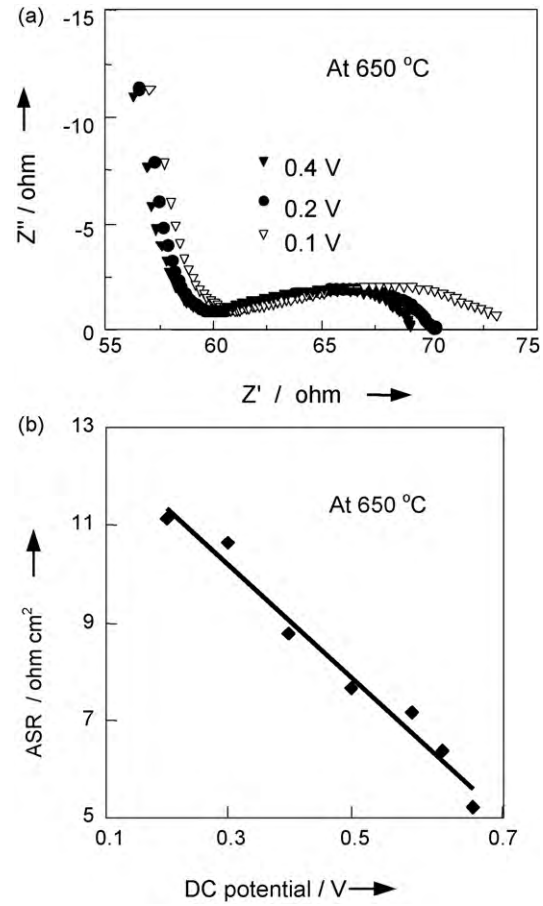

Fig. 16. (a) Complex impedance plots of cell-800 at 650 °C under different d.c. polarization potential and (b) variation of ASR with d.c. polarization potential.

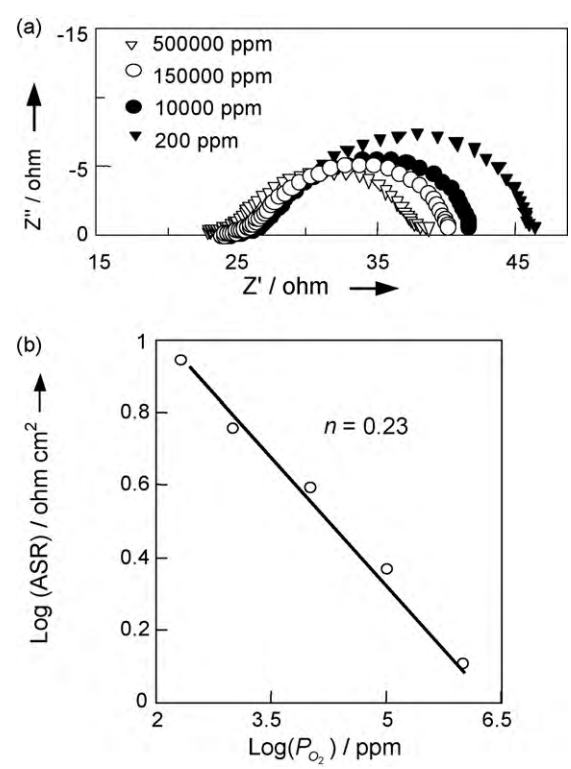

Fig. 17. (a) Complex impedance plots at 650 °C at different oxygen partial pressures and (b) variation of ASR with P_{O_2} for cell-800.

shown in Fig. 17(b) can be expressed as:

$$ASR = ASR_0(P_{O_2})^n \quad (10)$$

The value of n gives useful information about the type of species involved in the reactions at the electrode [30].

$$n = 1, \quad O_2(g) \Leftrightarrow O_{2,abs} \quad (11)$$

$$n = \frac{1}{2}, \quad O_{2,abs} \Leftrightarrow 2O_{abs} \quad (12)$$

$$n = \frac{1}{4}, \quad O_{abs} + 2e' + V_O^{\bullet\bullet} \Leftrightarrow O_O^x \quad (13)$$

The value of $n = 0.23$ estimated in the present study indicates the absorption of oxygen in the oxide lattice, giving rise to the formation of electrons and oxygen vacancies according to Eq. (13). The increase in concentration of such oxygen vacancies and electrons in the oxide lattice with increased P_{O_2} reduces the ASR (Fig. 17(b)).

The ASRs obtained in the present study is compared with the reported values in Table 2. A close scrutiny of Table 2 reveals that the $Nd_{1.8}Ce_{0.2}CuO_{4\pm\delta}$ cathode exhibits the lowest ASR compared with the cathodes reported earlier. The low ASR for $Nd_{1.8}Ce_{0.2}CuO_{4\pm\delta}$ in the present study is due to its nanocrystalline nature. In fact, the nanocrystalline material not only enhances the electrical conductivity, but also improves the electrode/electrolyte interface contact. Additionally, the surface-to-volume ratio increases and leads to increased surface area for catalytic activity. All these factors are responsible for the reduction in the ASR.

4. Conclusions

The combustion technique considerably reduces the sintering temperature and time and also yields nanostructured $Nd_{2-x}Ce_xCuO_{4\pm\delta}$ solid solutions. Solid solubility up to $x = 0.2$ is established by X-ray powder diffraction. The temperature-dependent conductivity exhibits a PTC to NTC transition at 625 °C for $Nd_{2-x}Ce_xCuO_{4\pm\delta}$ within the solid solubility limit. The $Nd_{1.8}Ce_{0.2}CuO_{4\pm\delta}$ cathode is thermochemically stable against GDC, though it reacts chemically with YSZ at high temperature. The catalytic activity of $Nd_{1.8}Ce_{0.2}CuO_{4\pm\delta}$ is established from an EIS study. Sintering of the symmetric cell at high temperature increases the ASR due to grain growth. $Nd_{1.8}Ce_{0.2}CuO_{4\pm\delta}$, prepared using the combustion technique, promises to be a potential cathode for ITSOFC applications.

Acknowledgments

The authors are thankful to UGC, New Delhi and DST, New Delhi for financial support through the SAP/DRS and FIST programs, respectively, to carry out this work. Ms. A. P. Khandale is grateful to UGC, New Delhi for the award of a Rajiv Gandhi fellowship (F14-2(SC)/2007(SA-III)).

References

[1] M. Dokiya, Solid State Ionics 152/153 (2002) 383–392.
[2] C. Chervin, R.S. Glass, S.M. Kauzlarich, Solid State Ionics 176 (2005) 17–23.
[3] H. Ullmann, N. Trofimenko, F. Tietz, D. Stöver, A. Ahmad-Khanlou, Solid State Ionics 138 (2000) 79–90.
[4] X.Y. Xu, C.R. Xia, G.L. Xiao, D.K. Peng, Solid State Ionics 176 (2005) 1513–1520.
[5] V.V. Kharton, A.P. Viskup, A.V. Kovalesvsky, E.N. Naumovich, F.M.B. Marques, Solid State Ionics 143 (2001) 337–353.
[6] X. Dong, Z. Wu, X. Chang, W. Jin, N. Xu, Ind. Eng. Chem. Res. 46 (2007) 6910–6915.
[7] D.J. Buttrey, P. Ganguly, J.M. Honig, C.N.R. Rao, R.R. Schartman, G.N. Subbanna, J. Solid State Chem. 74 (1988) 233–238.
[8] J.D. Jorgensen, B. Dabrowski, S. Pei, D.R. Richards, D.G. Hinks, Phys. Rev. B 40 (1988) 2187–2199.
[9] A. Mehta, P.J. Heaney, Phys. Rev. B 49 (1994) 563–571.
[10] M. Soorie, S.J. Skinner, Solid State Ionics 177 (2006) 2081–2086.
[11] X. Ding, X. Kong, J. Jiang, C. Cui, J. Hydrogen Energy 34 (2009) 6869–6875.
[12] A. Aguadero, J.A. Alonso, M.T. Fernandez, M.J. Escudero, L. Daza, J. Power Sources 169 (2007) 17–21.
[13] J. Wan, J.B. Goodenough, J.H. Zhu, Solid State Ionics 178 (2007) 281–286.
[14] M.J. Escudero, A. Aguadero, J.A. Alonso, L. Daza, J. Electroanal. Chem. 611 (2007) 107–116.
[15] M.A. Daraukh, V.V. Vashook, H. Ullmann, F. Tietz, I. Arual Raj, Solid State Ionics 158 (2003) 141–150.
[16] Q. Li, H. Zhao, L.H. Huo, L. Sun, X.L. Cheng, J.C. Grenier, Electrochem. Commun. 9 (2007) 1508–1512.
[17] V.V. Kharton, A.A. Yaremchenko, E.N. Naumovich, J. Solid State Electrochem. 3 (1999) 303–326.
[18] S.F. Palguev, V.K. Gilderman, V.I. Zemstov, High Temperature Oxide Electronic Conductors For Electrochemical Devices, Nauka, Mascow, 1990.
[19] A. Aguadero, J.A. Alonso, M.J. Escudero, L. Daza, Solid State Ionics 179 (11–12) (2008) 393–400.
[20] V.I. Voronin, A.E. Kar'kin, B.N. Goshchitski, Phys. Solid State 40 (2) (1998) 157–162.
[21] J.B. Goodenough, A. Manthiram, J. Solid State Chem. 88 (1990) 115–139.
[22] P. Ganguly, C.N.R. Rao, J. Solid State Chem. 53 (1984) 193–216.
[23] G. Spinolo, M. Scavini, P. Ghigna, G. Chiodelli, G. Flor, Physica C 254 (1995) 359–369.
[24] T.J.B. Holland, S.A.T. Redfern, Miner. Mag. 61 (1997) 65–77.
[25] J.S. Kim, E.P. Kvam, Physica C 292 (1997) 203–210.
[26] H. Takagi, S. Uchida, Y. Tokura, Phys. Rev. Lett. 62 (1989) 1197–1199.
[27] O.G. Singh, B.D. Padalia, O. Prakash, K. Suba, A.V. Narlikar, L.C. Gupta, Physica C 219 (1994) 156–161.
[28] K. Singh, S.A. Acharya, S.S. Bhoga, Ionics 12 (2006) 295–301.
[29] F. Mauvy, J.M. Bassat, E. Boehm, J.P. Manaud, P. Dordor, J.C. Grenier, Solid State Ionics 158 (2003) 17–28.
[30] E. Siebert, A. Hammouche, M. Kleitz, Electrochim. Acta 40 (1995) 1741–1753.